

高頻應用之砷化銦鋁/砷化銦鎵

變異結構高電子移動率電晶體之研究

研究生：連亦中

指導教授：張翼 博士

國立交通大學材料科學與工程研究所

摘要

本研究成功製作高頻應用之高效能砷化銦鋁/砷化銦鎵變異結構高電子移動率電晶體(MHEMTs)，並且對此元件做了深入的分析與探討。為了增進此變異結構高電子移動率電晶體之特性，在改善元件磊晶結構的同時，也研發出數種新穎的縮小閘極線寬的技術。另外，也對元件的高頻應用設計了元件的圖形佈局(Layout)與討論相關的電性量測技巧。

在論文中，研發出數種新的縮小閘極線寬的技術並且應用在MHEMT元件上。首先是使用深紫外光(DUV)微影配合特定角度乾蝕刻技術製作出具有0.15- μm 的 Γ 型gate之MHEMT，這是第一次發表的一種降低製作成本與手續的方法。用此方法製作的MHEMT具有680mA/mm的汲極-源極電流以及728mS/mm的高轉導值。此元件也展現了130GHz的高截止頻率(f_T)與180GHz的最高震盪頻率(f_{max})。另外，研發出利用熱回流技術與使用電子束雙層光阻製作出0.1- μm 的T型閘極，並且成功的應用在MHEMT元件製作上。跟一般的兩次電子束微影的閘極製作方法相比，與原先製程相容的熱回流技術具有製程簡單並且降低成本的優點。

在線寬縮小至100nm以下的部分，成功的在low-noise MHEMT元件上使用

介電材料sidewall方法製作出 90nm的T型閘極。此 160 μ m-width的MHEMT在 16GHz頻率之下的雜訊指數為 0.69dB且相對應的增益(associated gain)為 9.76dB。此外，具有 70nm的T型閘極與double δ -doping之power MHEMT元件也被成功的製作與研究。因具備奈米尺寸的閘極與銦含量高達 60%的通道層，此 MHEMT具有 890mA/mm的飽和汲極-源極電流以及 827mS/mm的轉導值，並展現 200GHz的高截止頻率(f_T)與 300GHz的最高震盪頻率(f_{max})。此元件在 32GHz之Ka頻段下具有良好的特性，表現出 14.5dBm的最大輸出功率對應 11.1dBm的P1dB，以及 9.5dB的功率增益。

另外，論文中也探討Ti/Pt/Cu閘極結構對於MHEMT中的砷化鋁銦(InAlAs)蕭特基層之電性與熱穩定性。與一般的Ti/Pt/Au作比較之後發現，此種具有銅金屬的蕭特基金屬結構在經過熱處理之後仍具有良好的特性。由材料分析得知，加熱到時在InAlAs上的Ti/Pt/Cu並沒有任何擴散的現象。加熱到 400°C之後，銅金屬才開始擴散並且與下層形成Cu₄Ti。此結果驗證了使用Pt作為擴散阻擋層的Ti/Pt/Cu結構具有高達 350°C的良好熱穩定性，並且可以應用在MHEMT元件與單石微波積體電路(MMICs)上。

The Study of InAlAs/InGaAs Metamorphic High Electron Mobility Transistors for High Frequency Applications

Student: Yi-Chung Lien

Advisor: Dr. Edward Yi Chang

Department of Materials Science and Engineering

National Chiao Tung University

Abstract

High performance InAlAs/InGaAs metamorphic high electron mobility transistors (MHEMTs) have been fabricated and characterized for high frequency applications. The performance of the MHEMTs was improved by optimizing the device structure and reducing the gate length using several novel gate-shrinking techniques. The epi-structure, layout design and electrical measurements of the MHEMTs were also discussed.

In this dissertation, several novel gate shrinking processes for MHEMTs fabrication were developed. For cost-effective production of submicron MHEMTs, a 0.15- μm Γ -shaped gate MHEMT technology using Deep UV lithography and a tilt dry-etching technique was developed and demonstrated for the first time. The fabricated 0.15- μm MHEMT using this novel technique shows a drain-source current of 680 mA/mm and transconductance of 728 mS/mm. The cutoff frequency f_T and maximum oscillation frequency f_{max} of the MHEMT are 130 GHz and 180 GHz, respectively. In addition, a 0.1 μm T-gate was achieved by thermally reflowing the bi-layer E-beam resist using hotplate and the 0.1- μm T-gate was applied to the MHEMT manufacture. Comparing with 2 step lithography of the conventional

E-Beam T-gate process, the reflowed gate process is a much simpler, relatively inexpensive and flexible process.

Under 100-nm scale, a low-noise MHEMT using 90-nm sidewall T-gate process was also successfully fabricated. The noise figure of the 160 μ m-width MHEMT was 0.69dB and the associated gain was 9.76dB at 16GHz. Moreover, a 70-nm In_{0.52}Al_{0.48}As/In_{0.6}Ga_{0.4}As power MHEMT with double δ -doping for power application was also fabricated and evaluated. The device has a high transconductance of 827 mS/mm, high saturated drain-source current of 890 mA/mm, high f_T of 200 GHz, and a high f_{max} of 300 GHz was achieved due to the nanometer gate length and the high Indium content in the channel. When measured at 32 GHz, the device demonstrates a maximum output power of 14.5 dBm with P1dB of 11.1 dBm and the power gain is 9.5 dB. The excellent DC and RF performance of the 70-nm MHEMT shows a great potential for the Ka band power applications.

In addition, electrical characteristics and thermal stability of the Ti/Pt/Cu contact on InAlAs Schottky layer of the MHEMT were investigated. The Ti/Pt/Cu Schottky contact had comparable electrical properties compared to the conventional Ti/Pt/Au contact after annealing. As judged from the material analysis, the Ti/Pt/Cu on InAlAs after 350°C annealing showed no diffusion sign into the InAlAs. After 400°C annealing, the interfacial mixing of Cu and the underlying layers occurred and resulted in the formation of Cu₄Ti. The results show that the Ti/Pt/Cu Schottky contact using platinum as the diffusion barrier is very stable up to 350°C annealing and can be used for the InAlAs/InGaAs HEMTs and MMICs fabrication.

誌 謝

本論文能夠順利的完成，首先要感謝我的博士班指導教授張翼博士。在我博士班的研究生涯中，他帶領我進入砷化鎵高頻元件的領域，並提供完整的訓練指導及充足的儀器資源，並使我能參與建立砷化鎵高頻應用之高電子移動率電晶體的製程。在張翼教授悉心指導之下，讓我了解提升研究水準與尋找正確研究方向的重要性，並且有機會參與國外知名學術單位合作的尖端研究計畫，拓展研究視野與世界觀。在交通大學材料科學與工程研究所的日子，也讓我感受到張翼教授幽默風趣並具有特色的指導方式與實驗室溫馨的研究氣氛，這個難得可貴的經歷與學習經驗，讓我受用無窮。

在這裡感謝實驗室的張晃崇博士與陳仕鴻博士，兩位學長耐心指導實驗方面寶貴的經驗與知識，使我減少許多摸索的時間。張晃崇博士積極的研究態度與陳仕鴻博士謙遜的個性，更是我該學習的部分。也要感謝李承士博士、李澤倫先生、王勝評先生、張尚文博士、楊宗熺博士、羅廣禮博士、方照詒博士在製程以及材料分析上提供幫助及建議，與在實驗和量測分析上面的幫忙。感謝國家奈米元件實驗室(NDL)及交大奈米中心(前半導體中心)，同時提供優良的儀器設備與環境，使實驗能夠更加順利進行。特別要感謝的是與張翼教授有合作關係之東京工業大學(TITech)的 Yasuyuki Miyamoto 教授以及 Takeshi Yamaguchi 先生，對我在日本東京做研究時的關心照顧以及實驗上的協助。

另外我也要感謝同窗多年的褚立新同學、謝炎璋同學、李晃銘同學，一起陪伴我走過五年多的博士班生活，不但在實驗室內討論實驗與互相鼓勵，閒暇之餘的歡樂相處也是寶貴的時光。感謝陳克弦同學、黃瑞乾同學、徐金鈺同學、吳偉誠同學、呂宗育同學、吳雲驥同學、陳俊淇同學在實驗上的幫忙，以及詹前璋先生在儀器設備及廠務方面的幫忙。感謝張家達同學、許立翰同學、林美璇同學、胡吟竹同學、Kartik 同學、黃珍樺同學、吳昶紋同學、林家慶同學、林博遠同學、

董福慶同學、曾建堯同學以及歷年來許多實驗室的夥伴默默的幫助我，也要謝謝蘇筠雯小姐及莊蕙菁小姐在行政上的協助幫忙。

特別要感謝的是張家源同學、郭建億同學以及已畢業的沈柏村同學、彭怡瑄同學與陳柏舟同學，在實驗室共同研究主題上的大力幫忙與互相討論，一起解決實驗上遭遇的問題與共同克服困難，使我能順利完成實驗並且可以保持研究的活力。

最後，我要特別感謝我的父母親家人與女友，感謝您們的關心、支持、包容與鼓勵，使我無後顧之憂，能夠專心順利完成學業。願這份榮耀與您們分享。



Contents

Abstract (in Chinese)	i
Abstract (in English)	iii
Acknowledge (in Chinese)	v
Contents	vii
Table Captions	x
Figure Captions	xi
Chapter 1 Introduction	1
1.1 General Background and Motivation.....	1
1.2 Overview of High Electron Mobility Transistors (HEMTs).....	1
1.3 Gate Shrinking Technologies.....	3
1.4 Outline of the Dissertation.....	4
Chapter 2 Fabrication of GaAs Metamorphic High Electron Mobility Transistors	12
2.1 Material Properties and Growth of MHEMT.....	12
2.2 Device Fabrication.....	13
2.2.1 Mesa isolation.....	13
2.2.2 Ohmic contact Formation.....	13
2.2.3 T-shaped gate and Recess process.....	14
2.2.4 Device passivation and contact via formation.....	15
2.3 Airbridge formation.....	15

Chapter 3 DC and RF Measurements of GaAs Metamorphic High Electron Mobility Transistors.....26

3.1 Device Characterization.....26

3.2 DC characteristics.....26

 3.2.1 I-V characteristics.....26

 3.2.2 Transmission line model (TLM).....28

 3.2.3 Breakdown characteristics.....29

3.3 RF Characteristics & Measurements.....29

 3.3.1 Scattering parameters.....29

 3.3.2 Current gain cutoff frequency f_T31

 3.3.3 Maximum frequency of oscillation f_{max}32

 3.3.4 Noise figure.....33

 3.3.5 RF measurement calibration.....36

3.4 Device Layout Designing.....36

 3.4.1 Effect of Pad Parasitics & De-embedding.....36

 3.4.2 Device Layout.....37

 3.4.3 Thru-Reflect-Line (TRL) calibration.....37

 3.4.4 RF measurement after TRL calibration.....38

Chapter 4 0.15- μm Γ -Shaped Gate $\text{In}_{0.52}\text{Al}_{0.48}\text{As}/\text{In}_{0.6}\text{Ga}_{0.4}\text{As}$ Metamorphic HEMTs Using DUV Lithography and Tilt Dry-Etching Technique.....55

4.1 Introduction.....55

4.2 Experimental.....56

4.3 Results and Discussion.....57

4.4 Conclusion.....59

Chapter 5 Low Noise Metamorphic HEMTs with Reflowed 0.1 μm

T-Gate.....65

5.1 Introduction.....	65
5.2 Experimental.....	66
5.3 Results and Discussion.....	67
5.4 Conclusion.....	68

Chapter 6 Characterization and Fabrication of Low Noise Metamorphic GaAs HEMTs Using 90nm Sidewall T-gate.....75

6.1 Introduction.....	75
6.2 Experimental.....	75
6.3 Results and Discussion.....	76
6.4 Conclusion.....	77



Chapter 7 High-Performance $\text{In}_{0.52}\text{Al}_{0.48}\text{As}/\text{In}_{0.6}\text{Ga}_{0.4}\text{As}$ Power Metamorphic HEMT for High Frequency Applications.....84

7.1 Introduction.....	84
7.2 Experimental.....	84
7.2.1 Fabrication of nano T-gate using E-beam lithography and tri-layer resist...85	
7.2.2 Improvements of resist profile and alignment precision for nano T-shaped gate lithography.....	86
7.3 Results and Discussion.....	87
7.4 Conclusion.....	88

Chapter 8 Thermal stability of Ti/Pt/Cu Schottky contact on InAlAs layer.....100

8.1 Introduction.....100

8.2 Experimental.....101

8.3 Results and Discussion.....102

8.4 Conclusion.....104

Chapter 9 Conclusion.....111

Reference.....113

Vita (in Chinese)

Publication List



Table Captions

Chapter 1

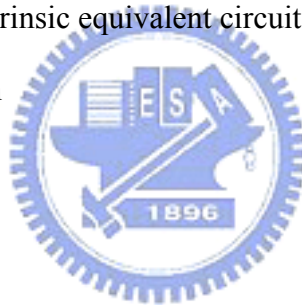
Table 1.1 Comparison of lattice-matched InP HEMT and metamorphic GaAs HEMT.

Chapter 5

Table 5.1 Summary of device performance of the MHEMT with non-reflowed and reflowed T-Gate.

Chapter 6

Table 6.1 The extrinsic and intrinsic equivalent circuit parameters of the MHEMT device of 160 μm of gate width



Chapter 8

Table 8.1. Barrier heights (ψ) and the ideality factors (n) of the Ti/Pt/Cu Schottky contact on InAlAs and the Ti/Pt/Au Schottky contact on InAlAs under various annealing temperatures.

Figure Captions

Chapter 1

Fig. 1.1 Conventional HEMT structure.

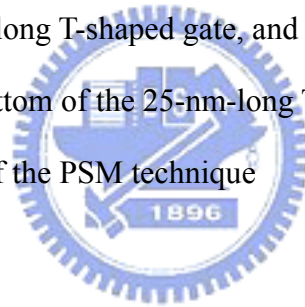
Fig. 1.2 Energy band gap v. s. lattice constant for $\text{In}_x\text{Al}_{1-x}\text{As}/\text{In}_y\text{Ga}_{1-y}\text{As}$ system.

Fig. 1.3 SEM photographs of the EB resist pattern for nanocomposite and conventional ZEP.

Fig. 1.4 Cleaved cross section of a 30-nm T-gate. Each material is specified in the figure.

Fig. 1.5 (a) Schematic cross-section view of the HEMT, (b) Cross-sectional TEM image of the 25-nm-long T-shaped gate, and (c) Magnification of the TEM image around the bottom of the 25-nm-long T-shaped gate.

Fig. 1.6 T-gate process flow of the PSM technique



Chapter 2

Fig. 2.1(a) Single δ -Doped structure for Low-Noise application

Fig. 2.1(b) Double δ -Doped structure for Power application

Fig. 2.2 Mesa Etching

Fig. 2.3 Ohmic photo

Fig. 2.4 Ohmic metal

Fig. 2.5 Ohmic window and ebeam T-gate followed by recess

Fig. 2.6 Gate metal deposition

Fig. 2.7 Passivation

Fig. 2.8 Nitride Via Etching

Fig. 2.9 TLM of the AuGe/Ni/Au Ohmic contact for MHEMT

Fig. 2.10 (a) The TLM patterns, (b) The illustration of utilizing TLM to measure the Ohmic contact resistance.

Fig. 2.11 The First Photolithography Barrier Layer V_i Spacer

Fig. 2.12 Thin Metals Ti/Au Deposition

Fig. 2.13 The Second Photolithography for Plating Area Channel

Fig. 2.14 Au electroplating

Fig. 2.15 After thin metal etching and PR Removal

Fig. 2.16 Photos of the Au airbridges of the device

Chapter 3

Fig. 3.1 Band diagrams at three different locations along the channel of a HEMT

Fig. 3.2 Actual characteristics and those predicted by Eq. (3-3)

Fig. 3.3 TLM pattern

Fig. 3.4 The illustration of utilizing TLM to measure ohmic contact resistance

Fig. 3.5 The equivalent two-port network schematic at low frequency

Fig. 3.6 The equivalent two-port network schematic at high frequency

Fig. 3.7 Small signal representation of a common source FET

Fig. 3.8 Definition of Cutoff Frequency f_T

Fig. 3.9 Short, through and loads for the calibration

Fig. 3.10 Effect of Pad Parasitics on h_{21} & f_T

Fig. 3.11 (a) Top-views of the A-type layout, and (b) C-type device layout

Fig. 3.12(a) coplanar waveguide structure designed at 94 GHz for the A-type layout using software, and (b) final designed A-type layout using the result of the simulation

Fig. 3.13 On-wafer TRL standards (Metal patterns on substrate) for A-type layout

Fig. 3.14 Measured S-parameters of REFLECT-Open

Fig. 3.15 Measured S-parameters of REFLECT-Short

Fig. 3.16 Measured S-parameters of LINE-1: 600um

Fig. 3.17 Measured S-parameters of LINE-2: 300um

Fig. 3.18 Check THRU after TRL Calibration, (a) the Smith chart of the S-parameter before and after TRL calibration, (b) magnitude and phase of S21

Fig. 3.19 Current gain h_{21} and MAG/MSG of MHEMT before and after TRL calibration, (a) H21 (1-110GHz) without TRL calibration, (b) Focus on 60-110GHz of H21 & MAG/MSG before and after on-wafer TRL calibration.

Chapter 4

Fig. 4.1 The deep UV lithography and tilt dry-etching process steps for fabricating the submicron Γ -shaped gate MHEMT. (a) Deep UV exposure, (b) selective development of the top layer, (c) tilt dry-etching of the bottom layer, and (d) Γ -shaped gate profile after gate metal lift-off.

Fig. 4.2 The cross-sectional SEM images of (a) 0.15- μm Ti/Pt/Au Γ -shaped gate, and (b) resist profile after the tilt dry-etching process.

Fig. 4.3 Critical dimension (C.D.) of the measured gate length (L_g) and the ideal gate length (L_{gi}) as a function of the tangent of the tilt angle θ .

Fig. 4.4 (a) Drain-source current vs. drain-source voltage curves, (b) transconductance vs. gate-source voltage, and (c) gate-drain breakdown voltage (V_{BR}) of the 0.15 μm Γ -shaped gate MHEMT.

Fig. 4.5 Input impedance (Z_{in}) vs. frequency from 1 to 40 GHz extracted from one-port forward-bias S-parameter measurement

Fig. 4.6 Frequency dependence of the current gain H_{21} , power gain MAG/MSG , and

unilateral gain U of the $0.15 \mu\text{m}$ Γ -shaped gate MHEMT. Frequency range was from 2 GHz to 65 GHz and device was biased at $V_{ds} = 1.5 \text{ V}$ and $V_{gs} = -0.7 \text{ V}$.

Chapter 5

Fig. 5.1 The SEM micrograph: (a) conventional E-beam resist and its $0.25 \mu\text{m}$ T-gate.

(b) the resist after shrinking by thermally reflow and its $0.1 \mu\text{m}$ T-gate.

Fig. 5.2 Transconductance of the $0.1 \mu\text{m} \times 160 \mu\text{m}$ MHEMT.

Fig. 5.3 Typical current gain H_{21} , MAG/MSG , and unilateral gain U as a function of frequency of the $0.1 \mu\text{m} \times 160 \mu\text{m}$ MHEMT.

Fig. 5.4 Noise Figure and associated gain as a function of frequency at $V_{DS} = 1 \text{ V}$ and $I_{DS} = 14 \text{ mA}$ of the $0.1 \mu\text{m} \times 160 \mu\text{m}$ MHEMT.



Chapter 6

Fig. 6.1 Scanning electron microscopy images: (a) Device layout with accomplished air bridges formed with $2 \mu\text{m}$ of plated Au, (b) and (c) show the T-gates under the Au air-bridges, (e) and (f) illustrate the cross sections of the $\text{SiN}_x/\text{SiO}_2$ sidewall T-gate profile.

Fig. 6.2 Transconductance (g_m) of the $160 \mu\text{m}$ -width MHEMT

Fig. 6.3 Typical current gain h_{21} , MAG/MSG , and unilateral gain U as a function of frequency of the $160 \mu\text{m}$ -width MHEMT

Fig. 6.4 Comparison between the calculated and measured S-parameters under $V_{ds} = 1.5 \text{ V}$ and $V_{gs} = -0.6 \text{ V}$

Fig. 6.5 Comparison between the calculated and measured S-parameters under $V_{ds} = 1.5 \text{ V}$ and $V_{gs} = -0.6 \text{ V}$

Chapter 7

Fig. 7.1 Cross-sectional SEM images of the (a) resist profile and the (b) 70-nm T-gate of the MHEMT.

Fig. 7.2 Process flow of fabricating of 50-nm T-shaped gate using E-Beam lithography and tri-layer resist.

Fig. 7.3 Cross sectional SEM image of the profile of tri-layer resist after E-beam lithography and development.

Fig. 7.4 Cross sectional SEM image of the 50-nm Ti/Au (100 nm/300 nm) T-shaped gate on InP substrate.

Fig. 7.5 (a) The photo of device pattern after E-Beam lithography. (b) The SEM image for the shifted gate pattern.

Fig. 7.6 Cross-sectional SEM image of the top opening (a) 200 nm, and (b) 450 nm for the tri-layer resist system.

Fig. 7.7 Cross-sectional SEM image of the optimal 50-nm T-shaped gate.

Fig. 7.8 Current-voltage characteristics of the $2 \times 40 \mu\text{m}$ MHEMT.

Fig. 7.9 Frequency dependence of the current gain (H_{21}) and MAG/MSG of the power MHEMT.

Fig. 7.10 Noise Figure (NF) of the $2 \times 40 \mu\text{m}$ MHEMT measured from 1 to 16 GHz.

Fig. 7.11 Measured 32-GHz power performance of the $4 \times 40 \mu\text{m}$ power MHEMT at drain bias of 2.5 V.

Chapter 8

Fig. 8.1. (a) I-V characteristics of the i-InAlAs/Ti/Pt/Cu Schottky diodes using HCl pretreatment with various annealing temperatures for 120 seconds, (b)

Barrier height vs. annealing temperature for the diodes with two different surface pretreatments.

Fig. 8.2. Auger depth profiles of the Ti/Pt/Cu on InAlAs (a) as deposited, (b) after annealing at 350°C for 30 minutes, and (c) after annealing at 400°C for 30 minutes.

Fig. 8.3. Cross-sectional TEM micrographs of the Ti/Pt/Cu on InAlAs layer (a) after 350°C annealing for 30 minutes, and (b) after 400°C annealing for 30 minutes.

Fig. 8.4. XRD results of Ti/Pt/Cu on InAlAs with various annealing temperatures for 30 minutes.

Fig. 8.5. EDX of the Ti layer of the InAlAsTi/Pt/Cu structure after annealed at (c) 350°C (d) 400°C for 30 minutes.

